JOURNAL OF combinatorial CHEMISTRY

Article

High-Throughput Synthesis and Screening of Hydrogen-Storage Alloys

Samuel Guerin, Brian E. Hayden, and Duncan C. A. Smith

J. Comb. Chem., **2008**, 10 (1), 37-43• DOI: 10.1021/cc700104s • Publication Date (Web): 12 December 2007

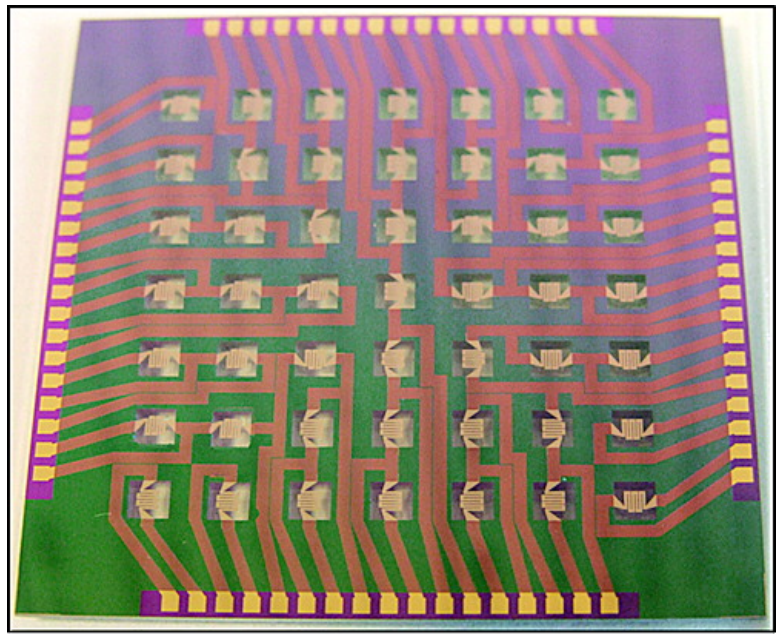

High-Throughput Synthesis and Screening of Hydrogen-Storage Alloys

Samuel Guerin,[‡] Brian E. Hayden,*[,†,‡] and Duncan C. A. Smith[‡]

School of Chemistry, University of Southampton, Southampton, SO17 1BJ, U.K., and Ilika Technologies Ltd., Kenneth Dibben House, Enterprise Road, University of Southampton Science Park, Chilworth, Southampton SO16 7NS, U.K.

Received June 27, 2007

Libraries of mixed-metal hydride materials are synthesized on a silicon microfabricated array of "hot-plate" MEMS devices, which allow high-throughput screening using temperature programmed desorption and infrared thermography. The heating plate of the MEMS device is a membrane with low heat capacity, allowing fast and localized temperature control and the extraction of calorimetric data from thermography. The combination of the synthetic method and screening chip allows a fast determination of the desorption temperature and hydrogen content of the materials. Mixed metal hydrides are synthesized directly. The potential of the method is exemplified by presenting results for the sorption properties of Mg_xNi_{1-x} hydride thin-film materials. The results are consistent with the literature, showing the highest hydrogen capacity and desorption temperature for the MgH_2 phase in Mg-rich compositions and the promotion of a lower temperature desorption from the Mg_2NiH_4 phase, with a concomitant reduction in hydrogen capacity.

1. Introduction

The discovery of a high capacity, energy efficient, and safe method of reversibly storing hydrogen for transportation is imperative in the development of a sustainable hydrogen economy. Mixed-metal hydride materials are considered to be a promising route to achieve such a goal. [1] These materials must be optimized to provide high gravimetric and volumetric hydrogen capacities. Favorable thermodynamic and kinetic properties to allow reversible hydrogenation at ambient temperatures and low pressures are also required. Cost, phase stability, and resistance to poisoning must be considered, along with good thermal conductivity, to prevent sintering in a dispersed form. Strategies to achieve these goals include modification of the base metal alloy; this is achieved through the synthesis of ternary and quaternary materials to produce optimal thermodynamic phases. Furthermore, catalyzing components can be added to improve the kinetics of the dissociative adsorption and associative desorption of molecular hydrogen at the surface. As a result of the number of parameters requiring optimization and the increasing number of compositional permutations with increasing alloy components, combinatorial synthetic and screening methods provide an ideal tool in the search for new hydrogen-storage materials.[2–4] While the range of mixed-metal hydrides is large,[5,6] aluminum- and magnesium-based alloys have received considerable attention because of their high gravimetric and volumetric hydrogen-storage capacities and their low cost. The major technical problem with these materials is that the temperature for hydrogen sorption is high, and dehydrogenation can be irreversible. Many studies have reported slight positive effects for variations in composition, such as substitution of the hydride-forming element and addition of catalytic elements. Examples include the addition of Ti to aluminum alloys,[2,7] addition of 3d transition metals to magnesium[8] and addition of nickel to magnesium hydride to form Mg_2NiH_4.[9] The latter system provides a good example of a material with a lowered desorption temperature ($\Delta T = -24$ K[10]) and reasonable gravimetric capacity (3.6 wt %) that has been studied extensively and will provide the benchmark for evaluating the new combinatorial methods described here.

Three combinatorial approaches have been reported for the synthesis and screening of hydrogen-storage materials,[2–4] and all have been carried out on sputtered metal alloy thin film materials which have subsequently been charged with hydrogen. Two[2,3] of the combinatorial screening techniques rely on changes in the optical response, as measured by the emissivity in the IR, or the optical transmission in the visible region, during the change from the metal to hydride, or hydride to metal, phase. The methods have the advantage of parallel screening for large combinatorial arrays, and the field is determined by the optical sample size on continuously graded thin films. The drawback is that only one key figure of merit; the hydrogenation/dehydrogenation temperature, is accessible. Screening in the third study[4] was carried out by X-ray microdiffraction, a sequential characterization which aimed at identification of structural phases rather than decomposition temperatures and storage capacity.

We have extended the high-throughput physical vapor deposition (HT-PVD) methodology recently developed[11] to control graded compositions of thin-film materials using molecular beam epitaxy (MBE) sources to directly synthesize

* To whom correspondence should be addressed. E-mail: beh@soton.ac.uk.
‡ Ilika Technologies Ltd.
† University of Southampton.

10.1021/cc700104s CCC: $40.75
Published on Web 12/12/2007

mixed-metal hydrides. This has been achieved by co-deposition of the metal elements in the presence of molecular hydrogen, or atomic hydrogen supplied by a plasma discharge source. The hydrides are deposited on a screening chip specifically designed to carry out fast sequential temperature programmed desorption and infrared thermography. Thin film calorimetry has been demonstrated using MEMS devices.[12,13] Because of the low thermal mass and fast heating rates of these devices, such MEMS devices can be successfully used as adiabatic calorimeters.[12] In addition, calibration of the microhotplate in the absence of an emissivity change should allow for the determination of the enthalpy change; this will be demonstrated in a further publication.

We show that the combination of TPD and MEMS-DSC can be used as a primary screen to obtain the temperature of desorption/dehydrogenation and the hydrogen capacity of the materials. Because this method relies on high heating rates (in the range of $1-57$ K s^{-1}) to detect desorbing hydrogen with sufficient sensitivity, the desorption of hydrogen is kinetically limited, and measurement near equilibrium is not possible. Existing high-throughput methods applied to hydrogen storage allow for calculation of thermodynamic properties, for example screening through emissivity[3] or optical changes.[14] In contrast, the method demonstrated here enables the calculation of hydrogen capacities and kinetic parameters such as activation energies. The figure of merit such as onset temperature and capacity, although measured under kinetic limitations, provide a direct measure of the trends observed under equilibrium conditions in the literature. We will show that the technique demonstrated provides a powerful rapid primary screen to survey a compositional space for interesting hydrogen-storage materials.

2. Experimental Section

The MgNi hydrides were deposited using an HT-PVD system described in more detail elsewhere.[11] Mg and Ni were deposited from an effusion and e-beam source, respectively, in a four-source ultrahigh vacuum (UHV) growth chamber with a base pressure of 1×10^{-10} mBar. Magnesium (4 mesh Mg turnings 99.98% from Alfa Aesar) was deposited from a normal temperature effusion source (DCA, $T_{max} = 1400$ °C, crucible volume 40 cm^3), and nickel (Ni shot, 99.95+% from Alfa Aesar) was deposited from an e-beam evaporator (crucible volume 40 cm^3, model SIHF-270-single earth from Temescal). Pyrolytic boron nitride and pyrolytic graphite crucibles were used for the magnesium and nickel sources, respectively. The "wedge" shutters and deposition rates were used to control the compositional range of the deposited material. The elements were simultaneously deposited at a rate of ~2.5 nm min^{-1} in the presence of molecular hydrogen (N5.5 hydrogen, Air Products) at 6×10^{-6} mBar at ~300 K. It was apparent from our measurements that it was not necessary to predissociate the hydrogen in a plasma source during the synthesis of the MgNi hydrides. Presumably this is because Ni is effective in catalyzing the dissociation of hydrogen sufficiently quickly to ensure hydride formation under the synthesis conditions.[15] In the case of pure Mg, the hydride was synthesized using a flux of atomic hydrogen from a plasma discharge source (MATS30, Mantis). A contact mask was used to ensure deposition was restricted to the microhotplates. The composition of the library was measured using macro-controlled energy dispersive spectroscopy (JSM 6500F thermal field emission scanning electron microscope fitted with Oxford Inca 300 EDS system). An example of the compositional gradient achieved using the wedge shutters is shown in Figure 1 and is characterized as expected for a binary system by a compositional variation in one direction and constant composition in the orthogonal direction. Samples for ex situ X-ray diffraction were prepared with an additional palladium cap layer (~10 nm, 99.95% Pd from Goodfellows) deposited from an e-beam source with a pyrolytic graphite crucible. Diffraction was carried out on a Bruker C2 Gadds X-ray diffractometer.

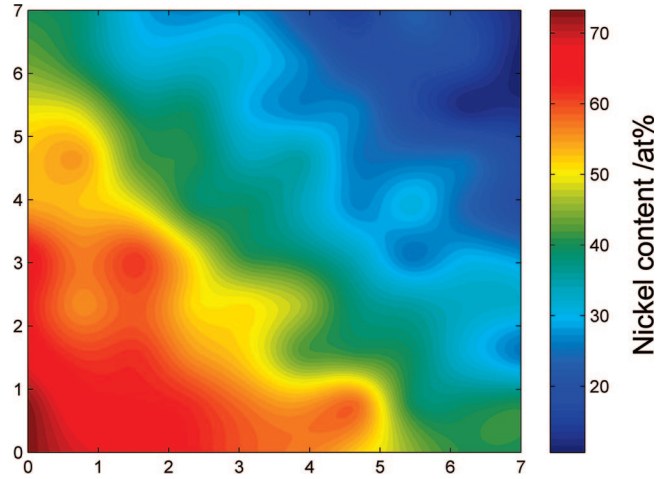

Figure 1. A typical compositional map of a library measured by energy dispersive spectroscopy; composition is given in atomic percentage (at. %). The nickel composition across the library ranges between 14 and 73 at. %.

The substrates $(\sim 32 \text{ mm})^2$ used for general characterization of material growth were silicon nitride-covered silicon (200 nm LPCVD Si_3N_4 on 50 nm thermally grown SiO_2). Once the growth conditions were optimized, the graded material was deposited via a contact mask onto a 7×7 microhotplate array, shown in Figure 2. Similar microhotplate arrays have been used as substrates for materials exploration[16] and for the development of gas-sensor arrays.[17–19] The development of single microelectromechanical system (MEMS) devices, incorporating a thin membrane combined with a platinum heater (simultaneously used as a temperature-resistance thermometer) for DSC measurement, has also been reported.[20,21] The arrays designed together with AML of Didcot, Oxon, U.K. used in this study are based on MEMS devices used more conventionally in planar pellistor sensor applications [22,23] which have been shown to be capable of achieving very high temperatures quickly, with low thermal cross talk between individual hotplates. The array (Figure 2) is silicon microfabricated, consisting of 49 MEMS hotplates in a 7×7 matrix. Each hot-plate comprises a 1 μm thick continuous silicon nitride membrane $(2 \times 2 \text{ mm})^2$, which has been fabricated through a back etch of the silicon substrate. Embedded in the center of each membrane is a 160 nm thick platinum serpentine track $(1 \times 1 \text{ mm})^2$ used

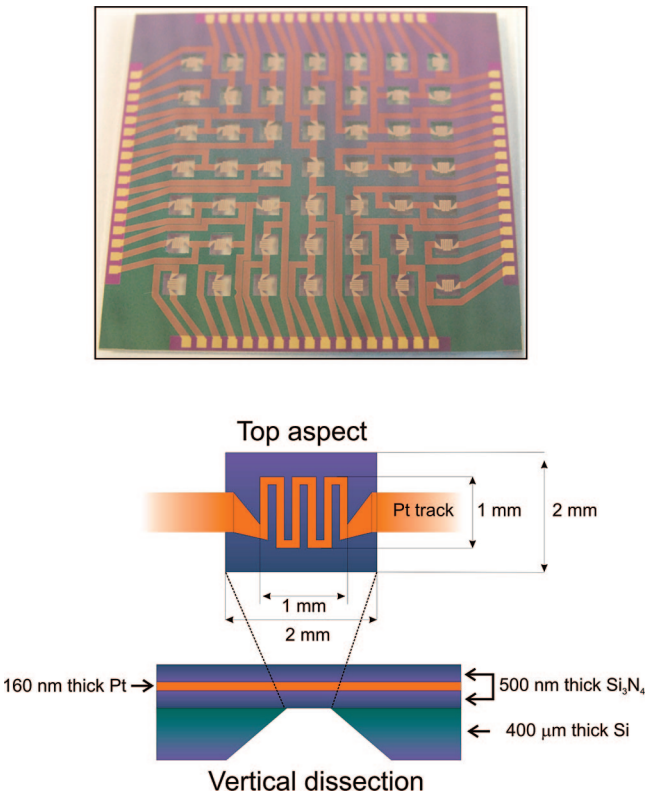

Figure 2. A photograph of the microhotplate array (top), consisting of a 7 × 7 grid of microhotplates. Contact is made to the platinum serpentine heater tracks via the 64 gold contacts around the edge of the array. Each microhotplate (below) consists of a platinum serpentine heater (160nm) on a 10 nm aluminium seed layer. The heater and electrical interconnect is sandwiched between Si_3N_4 membranes which are exposed around the heating fields by back etching the silicon substrate.

for heating. Each of the 49 MEMS heaters are independently controllable, with electrical contact being achieved through contact pads at the edge of the chip. The UHV holder provides electrical contact to the edge contacts on the chip, and 100 UHV electrical feed-throughs provide external control.

Calibration of the hot-plate temperature as a function of applied potential was achieved using an infrared thermal camera (Jade III, CEDIP, Paris) incorporating an InSb detector and with a spectral range of 3.6–5.1 μm, a resolution of 320 × 240 pixels, and a sensitivity of 20 mK. A 3.99 μm narrow band-pass filter was used for high-temperature imaging, and the images were captured through a CaF_2 window. For calibration, the heated fields of an array were carbon coated (using a suspension of graphitic carbon in *n*-propanol) to approximate blackbody emissivity. Calibrations were obtained for heating at ambient pressures and under vacuum conditions. Further calibration of the hot-plate temperature as a function of the applied potential was carried out, using the change in the resistance of the platinum track, a methodology previously demonstrated for such MEMS devices.[22] The linear temperature coefficient of resistance α was first determined by heating the devices in an oven while recording the resistance (Fluke 83). Five different devices across three arrays were measured. The value of α was determined to be 1.3 ± 0.25 × 10^{-3} K^{-1}. It was then possible to determine the temperature of the hot-plate, using

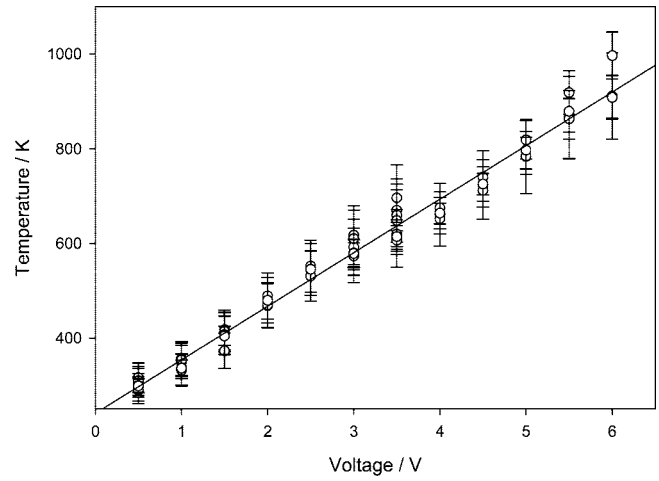

Figure 3. Plot of temperature vs voltage applied microhotplate for the three methods used. Linear regression performed on the resistance data set yields the line shown, which has a gradient of 114 K V^{-1} and an R^2 value of 0.999. Error bars of ±5% are shown.

this value, by measuring its resistance; the temperature of the hot plate can then be calculated using the temperature dependent expression for the resistance of metals[22]

$$R_H(T) = R_0[1 + \alpha(T - T_a)] \quad (1)$$

where R_H is the resistance of the hot plate at temperature T and R_0 is the resistance at ambient temperature T_a. The temperature of four hot plates was determined as a function of applied potential at a base pressure of 1 × 10^{-9} mBar. Resistance measurements were carried out using a Wheatstone bridge constructed with two 100 Ω resistors (RS Components), a 0.1–1000 Ω variable resistor (H. Tinsley & Co. Ltd., London), and a single hot plate.

Figure 3 shows the combined data from the pseudo-blackbody measurements and the resistance measurements. The relationship between the voltage applied to the heaters and the temperature of the heated field is linear (R^2 value of 0.999) in the range 310–1015 K with a gradient of 114 K V^{-1}. Temperatures of the hotplates are highly reproducible between the MEMS devices on an array: The error in absolute temperature is estimated at ±50 K, and that for the relative temperatures is estimated to be ±2 K. The maximum temperature achievable on the array field was ∼982 K; the temperature variation within the desorption field was ∼10%, and thst of the optical field of thermometry was ∼5%.

Screening was carried out in a UHV analysis chamber and high pressure cell (Figure 4), attached to the synthesis chambers via a transport system and masking station[11] which allows the synthesized materials to be transported under UHV conditions for screening without contamination. Each of the microhotplates was heated sequentially, while the hydrogen partial pressure and infrared images were recorded. The hydrogen partial pressure was recorded using a quadrupole mass spectrometer (Analyzer 100D, ESS, UK), with a dwell time of 1 ms. Infrared images were recorded using the infrared camera. The potential across each of the hotplates was increased at a rate of between 0.05 and 0.5 V s^{1-} corresponding to heating rates in the range 6–60 K s^{1-}. The potential was increased from 0 to 6 V; it was held at this

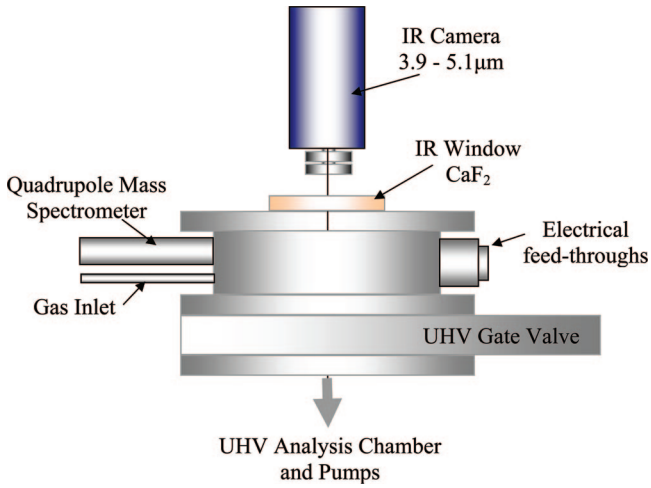

Figure 4. Schematic of the analysis chamber. The array is transferred into the environmental chamber in an array mount, using a manipulator (not shown for clarity). The array mount is plugged into a receiving cradle which enables electrical connection via the multiple UHV feed-through.

value for ~20 s, and then decreased at the same rate. These potentials were controlled using two analogue output cards and in-house software, written in LabView. The results were analyzed using in-house routines within the MATLab software suite.

There are, in principle, conflicting requirements of the heating plates for carrying out TPD and adiabatic calorimetric measurements using thermography: A linear heating rate is ideal for the former, but deviations from linearity because of enthalpy changes are essential for the latter. We show that the errors associates with deviations in linearity associated with the endotherm in dehydrogenation is smaller than errors associated with errors caused by inhomogeneous heating of the fields during TPD. In addition, the special localization of the thermographic measurement in a small part of the field results in a high sensitivity of the calorimetric measurement.

3. Results and Discussion

3.1. Temperature Programmed Dehydrogenation. A series of temperature programmed desorption (dehydrogenation) spectra for 21 fields of Mg_xNi_{1-x} (x = 0.86–0.37) hydrides is shown in Figure 5. Each field comprises a thin film of 120 nm (measured by AFM), the size of each field is 1 × 1 mm, The heating rate used was 57 K s^{-1}. At the highest temperatures achievable on the hot plate arrays (~980 K), not all the hydride has decomposed at these heating rates, both the time and temperature dependence of the decomposition is plotted in Figure 5. In the limit of very low Mg compositions, a relatively small single decomposition peak is observed at 580 K. Increasing the Mg content of the material leads to the appearance of an additional decomposition at higher temperature, an apparent increase in the intensity of the low temperature peak, and an increase in the total integral of desorbed hydrogen. At the highest Mg concentrations studied, the low temperature peak has become a low temperature shoulder on the overall decomposition profile. The onset temperature of decomposition remains relatively constant throughout the compositional range at

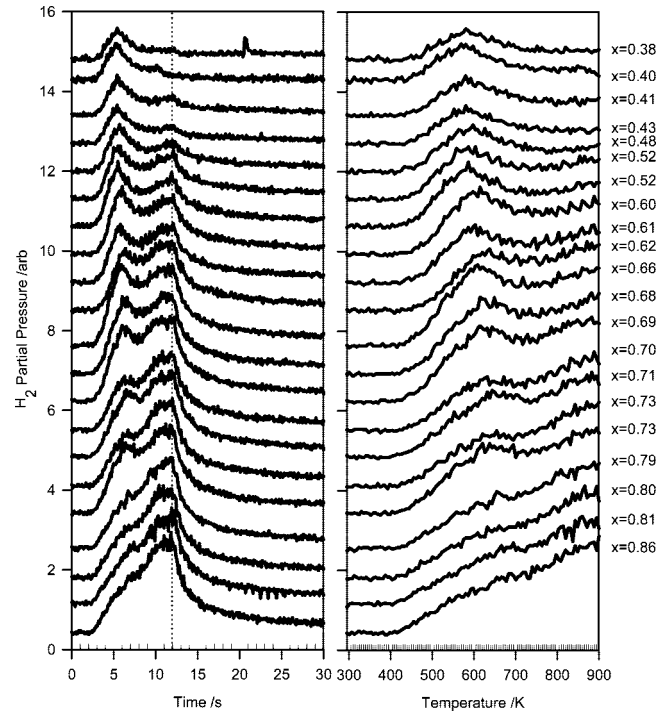

Figure 5. Desorption spectra from 21 fields of the Mg_xNi_{1-x} (x = 0.86–0.38) hydride shown as a function of time and temperature. Low nickel content samples exhibit two peaks merged together (14 at% Ni). As the nickel content is increased, the first peak increases in magnitude and shifts to shorter time (and lower therefore lower temperature). The second peak decreases in magnitude and disappears at 78 at. % Ni. A heating rate of 57 K s^{1-} and a maximum temperature of 982 K was used throughout this experiment. Heating stops at 12 s.

~470 K. The apparent high-temperature "peak" in the time plots is deceiving because the hotplates would not allow heating beyond 980 K, and the maximum in the decomposition/time curve corresponds to the end of the heating ramp: the temperature of the hotplate was kept constant at this maximum temperature, and the decomposition rate subsequently decreased. The heating rates are too high to allow decomposition of the hydride without significant desorption of the magnesium in MgH_2.[24] The MgH_2 decomposition is not taking place under equilibrium conditions because of the activation barrier and hence appears at significantly higher temperatures than would be expected at equilibrium (~552 K [10]). The effect of the addition of Ni to Mg is a significant reduction in the mean desorption temperature (Figure 5), with a concomitant decrease in the total amount of hydrogen desorbed (Figure 6). It will be shown that this increased desorption kinetics is caused by the formation of the Mg_2Ni hydride phase. The total amount of hydrogen desorbed by the thin film shown in Figure 6 has been calculated from the integral of the desorption peaks in Figure 5. Combination of the resulting desorption flux with the hydrogen pumping speed of the chamber, which has been determined experimentally, allows us to establish the absolute amount of hydrogen desorbed from the field. The latter, combined with the film thickness, provides a measure of the weight percentage of hydrogen in the metal hydride, and this is plotted in Figure 6.

The results in Figure 6 are plotted together with the curve which represents the expected storage capacity across the

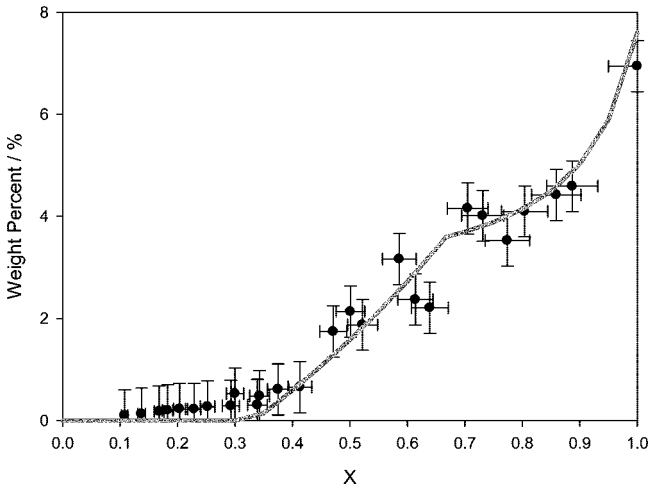

Figure 6. Total H_2 weight percent vs temperature determined from the integral of the desorption/time curves as a function of x for $Mg_xNi_{(1-x)}$. The trend in the total weight percent matches the trend observed in the simple model system. The plot is made up of three different arrays. The error bars shown are ±2.5% in x and ±5% in the integral.

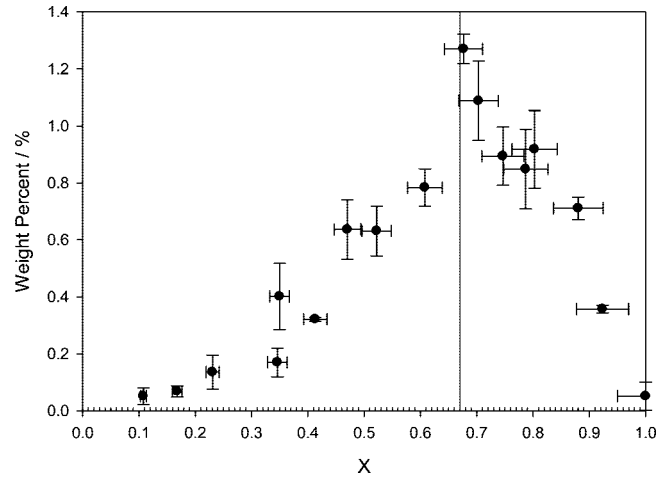

Figure 7. Total H_2 weight percent vs temperature below 775 K determined from the integral of the desorption/time curves as a function of x for $Mg_xNi_{(1-x)}$. The solid line denotes the position of Mg_2NiH_4 phase.

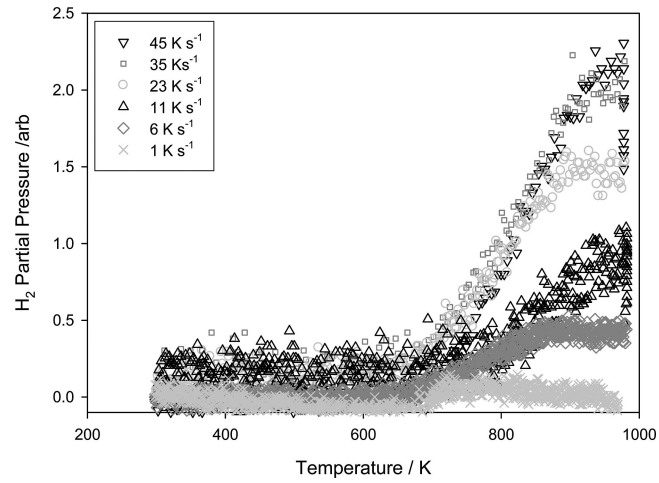

Figure 8. Examples of desorption spectra from six fields of the Mg hydride shown as a function temperature. Heating rates of between 1 and 45 K s^{-1} were used throughout this experiment, with a maximum temperature of 982 K.

composition range for the MgNi hydride system. The phases expected would be Ni, $MgNi_2$, Mg_2NiH_4, and MgH_2, with hydrogen-storage capacities of 0, 0, 3.6, and 7.6 wt %, respectively. [25] The results of the TDP experiment are clearly consistent with the expected capacity across the complete compositional range. We can conclude from these "benchmarking" experiments that (1) the synthesis method was capable of accessing the thermodynamically expected hydride phases and (2) that the TPD-MEMS hotplate array screening method is sufficiently sensitive and accurate to provide quantitative storage capacity data for the synthesized hydrides. The TPD data (Figure 5) also provide an immediate qualitative indication of decomposition kinetics as a function of composition. The results presented in Figures 5 and 6 also exemplify the efficacy of the screening methodology for the discovery of new potential hydrogen storage alloys. The binary compositional dependence of storage capacity and the basic trends in accessibility of the absorbed hydrogen (the desorption temperature) are obtained from the results of materials made on just three arrays. Note that the number of results potentially obtained the 49 fields of each single array was not realized in these experiments because of the misalignment of contacts within the UHV sample holder. The design of the sample holder is currently undergoing optimization, and the next generation will allow heating of all 49 fields in every experiment.

To assess the hydrogen capacity of the metal hydride material as a function of composition in a lower-temperature regime (at temperatures where the decomposition of any MgH_2 should not take place), desorption capacity at a limited maximum temperature becomes a relevant figure of merit. For the MgNi system, the amount of hydrogen desorbed up to 775 K has been evaluated from integration of the desorption flux below 775 K, and this is shown in Figure 7 as a function of alloy composition. This temperature is chosen because it should reflect the hydrogen capacity provided primarily by the phase (Mg_2NiH_4) responsible for the low-temperature desorption peak. The maximum in capacity associated with this figure of merit corresponds to the optimal composition for the Mg_2NiH_4 phase, as one would expect, and is again consistent with the four-phase model ($MgH_4-Mg_2NiH_4-MgNi_2-Ni$) predicted for this system. At the maximum temperature of desorption (775 K) under these conditions, desorption from the MgH_2 does not yet take place, and the $MgNi_2$ and Ni phases contain no hydrogen. Note that the maximum in the weight percent obtained in these measurements does not correspond to the expected value of 3.6 wt % because at these heating rates decomposition of the Mg_2NiH_4 phase is not complete even at 775 K.

3.2. Determination of Kinetic Parameters. A series of temperature programmed desorption (dehydrogenation) spectra for six fields of Mg hydrides is shown in Figure 8. Each field comprises a thin film of 80 nm (measured by AFM); the size of each field is 1 × 1 mm. Temperature programmed desorption was carried out at rates between 1 and 45 K s^{-1}. By variation and observation of the change in peak position, it was possible to determine the activation energy of the decomposition process. The activation energy for this process

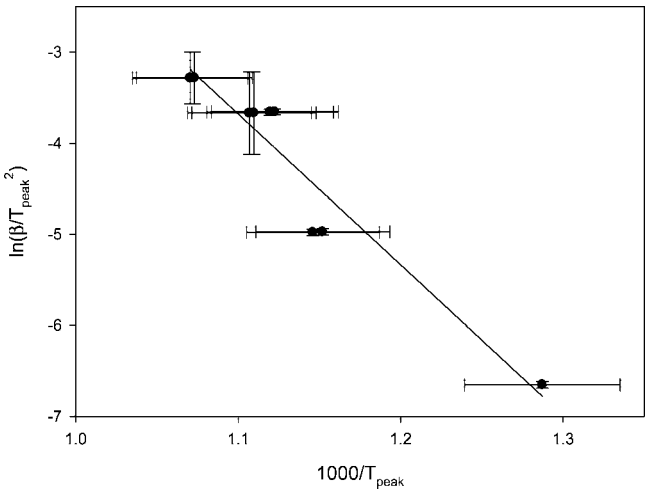

Figure 9. Plot of $1000/T_{peak}$ vs $\ln(\beta/T\text{peak}^2)$ for the decomposition of magnesium hydride at heating rates between 1 and 45 K s^{-1}. The error bars are based on an error in the peak position of ±30 K. The linear regression shown has an R^2 value of 0.92.

was determined by plotting $1000/T_{peak}$ versus $\ln(\beta/T_{peak}^2)$, where β is the heating rate and T_{peak} is the maximum in the desorption profile, Figure 9.[26] The activation energy as determined by this method is 142 ± 28 kJ mol^{-1}, based on an error in the peak position of ±30 K. This values falls into the center of the range of values observed for the activation energy for magnesium hydride decomposition in the literature (100–299 kJ mol^{-1}).[27]

3.3. Infrared Thermography. A continuous $Mg_xNi_{(1-x)}$ thin film was produced in the range of $x = 0.04$–0.53. The thickness of the film varied between 16.5 and 52.8 nm, measured by non-contact atomic force microscopy. Temperature programmed desorption was carried out as described above, at a heating rate of 57 K s^{-1}. Simultaneously, infrared images were recorded of the thin films during heating; these were recorded at a capture rate of 25 Hz, an integration time of 400 μS corresponding to an image being recorded every 2.4 K. The thermal response of the central region of the MEMS device was analyzed: a region of the image corresponding to 8 × 8 pixels was averaged, and this corresponded to an area of the field of approximately (0.5 mm).[2] The temperature (measured with the IR camera) versus time data was differentiated using a moving average method to yield the temperature flux versus time curves with a resolution of ~11 K. The result for the measurement of the field corresponding to the mixed-metal hydride composition $Mg_{0.65}Ni_{0.35}$ is shown in Figure 10.

The loss of hydrogen from metal hydrides is often accompanied by a drop in the Fermi energy E_f. This drop is associated with a loss of the bonding states between the hydrogen and the materials electrons.[3] The shift in E_f to a higher density of states leads to a more metallic and therefore more conductive material. This change in electrical properties is accompanied by a change in optical properties.[2,3,24,25] As the material is heated, the hydride decomposes to yield to the binary metal alloy, which has a lower emissivity. Because the heating rate is constant and known, we can estimate the emissivity of the material at each plateau. The first plateau gives an emissivity value of 0.75, and the second plateau gives an emissivity value of 0.32. This large change in

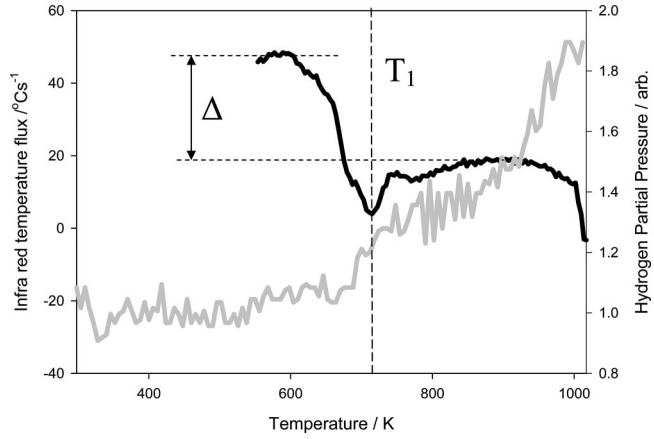

Figure 10. Simultaneous thermography (dark curve) and temperature programmed desorption (light curve) from a field with composition $Mg_{0.65}Ni_{0.35}H_y$. The result of the thermography shows that both the emissivity change associated with the decomposition of the hydride (Δ) and the exotherm associated with the decomposition (T_1) is observed. The latter is concomitant with the desorption peak in TPD associated with the Mg_2NiH_4 decomposition.

emissivity ($\Delta\epsilon = 0.43$) is of the same order as that calculated for hydrogen intercalation into different materials for electrochromic devices.[26]

Superimposed upon this emissivity change is the endotherm associated with the loss of hydrogen from the $Mg_{0.65}Ni_{0.35}$. This endotherm occurs at the same temperature (~720 K) as the first desorption peak (Figure 10) in the corresponding TPD data and, like the peak, is associated with the decomposition of the Mg_2NiH_4 phase.

In the case of the MgNi hydride system, the IR thermography was complicated by the fact that at the heating rates used, there was significant loss (sublimation) of magnesium during the decomposition of the hydride. We were therefore unable to extract quantitative thermodynamic quantities associated with discrete hydride phase decompositions. The method is now being optimized for lower heating rates and applied to base compositions that remain unchanged during the decomposition.

The endothermic heat transfer during the hydride decomposition results in changes in effective heating rate during the phase transition. This, in principle, can influence the accuracy of the TPD measurement, which relies on a linear heating rates throughout desorption. From Figure 10, one can see that the observed change in heating rate is large enough to enable the extraction of the flux. However, the maximum deviation in temperature (e.g., at T_1 in Figure 10) resulting from the endotherm is 5–7 K, depending on the contribution assumed because of emissivity changes. The measurement in Figure 10 has been made by integration over most of the desorption field. This deviation is much smaller than that associated with inhomogeneous temperatures over the complete field ±50 K. This small error will only contribute to deviations in maximum desorption peak temperatures or onset temperatures from the TPD measurement. Because hydrogen capacity is derived from integration of the desorption flux/time curve, there is no influence of these small deviations in temperature on capacity calculations.

4. Conclusions

A high-throughput synthetic and screening method has been developed for optimization of metal hydride storage materials. Results are presented for the screening of a benchmark binary hydride system, MgNi hydride, to validate the methodology. The hydride materials are synthesized by simultaneous deposition of elemental Mg and Ni in either a molecular or plasma atom source of hydrogen. A silicon microfabricated MEMS array with 49 independent heaters allows both temperature programmed desorption (TPD) and infrared thermography measurements. The integral of the TPD provides a measure of the hydrogen storage capacity as a function of composition. The results are consistent with the known phases of the MgNi hydride system, [28] demonstrating the validity of both the synthesis and screening method. The increased kinetics associated with the Mg_2NiH_4 phase is also evident from the decomposition temperature.

While the primary screen described here clearly operates away from the equilibrium limit achieved in other optical screens,[3,14] the additional information of storage capacity and clear trends in the kinetics of decomposition which are clearly relevant to practical storage materials demonstrate the effectiveness of the methodology. The apparent decomposition kinetics may be associated with the decomposition of the hydride itself or limited by hydrogen recombination at the surface. The technique provides a powerful rapid primary screen to survey a compositional space for interesting hydrogen storage materials. It also provides a method for obtaining the kinetic parameters explicitly when used as a secondary screen and varying heating rates in the range between 1 and 45 K s^{-1}. We show this by measuring the activation energy associated with the decomposition of magnesium hydride, 142 ± 28 kJ mol^{-1}, a result consistent the literature.

The method described can also be applied to screen hydride materials formed from the alloys by exposure to hydrogen at high pressure, and indeed, a 10 bar high-pressure cell has recently been tested in the laboratory. This will allow an assessment of the reversibility of the hydriding process.

Acknowledgment. We would like to acknowledge financial support from Ilika Technologies and support under the U.K. JIF scheme for the establishment of the experimental infrastructure at the University of Southampton.

References and Notes

(1) Schlapbach, L.; Zuttel, A. *Nature* **2001**, *414*, 353–358.
(2) Gremaud, R.; Borgschulte, A.; Chacon, C.; Van Mechelen, J. L. M.; Schreuders, H.; Zuttel, A.; Hjorvarsson, B.; Dam, B.; Griessen, R. *Appl. Phys. A: Mater. Sci. Process.* **2006**, *84*, 77–85.
(3) Olk, C. H. *Meas. Sci. Technol.* **2005**, *16*, 14–20.
(4) Garcia, G.; Domenech-Ferrer, R.; Pi, F.; Rodriguez-Viejo, J. *J. Comb. Chem.* **2007**, *9*, 230–236.
(5) Sandrock, G. *J. Alloys Compd.* **1999**, *293–295*, 877–888.
(6) Grochala, W.; Edwards, P. P. *Chem. Rev.* **2004**, *104*, 1283–1315.
(7) Bogdanovic, B.; Schwickardi, M. *J. Alloys Compd.* **1997**, *253–254*, 1–9.
(8) Vegge, T.; Hedegaard-Jensen, L. S.; Bonde, J.; Munter, T. R.; Norskov, J. K. *J. Alloys Compd.* **2005**, *386*, 1–7.
(9) Reilly, J. J.; Wiswall, R. H., Jr. *Inorg. Chem.* **1968**, *7*, 2254–2256.
(10) Hydpark-Database, Sandia National Laboratory.
(11) Guerin, S.; Hayden, B. E. *J. Comb. Chem* **2006**, *8*, 66–73.
(12) Lai, S. L.; Ramanath, G.; Allen, L. H.; Infante, P. *Appl. Phys. Lett.* **1997**, *70*, 43–45.
(13) Lopeandia, A. F.; Rodriguez-Viejo, J.; Chacon, M.; Clavaguera-Mora, M. T.; Munoz, F. J. *J. Micromech. Microeng.* **2006**, *16*, 965–971.
(14) Dam, B.; Gremaud, R.; Broedersz, C.; Griessen, R. *Scr. Mat.* **2007**, *56*, 853–858.
(15) Harris, J.; Andersson, S. *Phys. Rev. Lett.* **1985**, *55*, 1583.
(16) Taylor, C. J.; Semancik, S. *Chem. Mater.* **2002**, *14*, 1671–1677.
(17) Suehle, J. S.; Cavicchi, R. E.; Gaitan, M.; Semancik, S. *IEEE Electron Device Lett.* **1993**, *14*, 118–120.
(18) Cavicchi, R. E.; Suehle, J. S.; Chaparala, P.; Kreider, K. G.; Gaitan, M.; Semancik, S. In *Proceedings of the 1994 Solid State Sensor and Actuator Workshop*; Hilton Head, S.C., June 6−9; Institute of Electrical and Electronics Engineers: New York, 1994; pp 53−56
(19) Semancik, S.; Cavicchi, R. E.; Kreider, K. G.; Suehle, J. S.; Chaparala, P. *Sens. Actuators, B* **1996**, *34*, 209–212.
(20) Spassov, T.; Solsona, P.; Bliznakov, S.; Surinach, S.; Baro, M. D. *J. Alloys Compd.* **2003**, *356*, 639–643.
(21) Efremov, M. Y.; Olson, E. A.; Zhang, M.; Lai, S. L.; Schiettekatte, F.; Zhang, Z. S.; Allen, L. H. *Thermochim. Acta* **2004**, *412*, 13–23.
(22) Pike, A.; Gardner, J. W. *Sens. Actuators, B* **1997**, *45*, 19–26.
(23) Bartlett, P. N.; Guerin, S. *Anal. Chem.* **2003**, *75*, 126–132.
(24) Ostenfeld, C. W.; Davies, J. C.; Vegge, T.; Chorkendorff, I. *Surf. Sci.* **2005**, *584*, 17–26.
(25) Orimo, S.; Fujii, H. *Appl. Phys. A: Mater. Sci. Process.* **2001**, *72*, 167–186.
(26) Kissinger, H. E. *Anal. Chem.* **1957**, *29*, 1702–1706.
(27) Jensen, T. R.; Andreasen, A.; Vegge, T.; Andreasen, J. W.; Stahl, K.; Pedersen, A. S.; Nielsen, M. M.; Molenbroek, A. M.; Flemming, B. *Int. J. Hydrogen Energy* **2006**, *31*, 2052–2062.
(28) Gross, K. J.; Spatz, P.; Zuttel, A.; Schlapbach, L. *J. Alloys Compd.* **1997**, *261*, 276–280.

CC700104S